RESEARCH ARTICLE

Endmember Estimation Using Fuzzy Grade of Membership and Spectral Matching

M. R. VIMALA DEVI[ID] AND S. KALAIVANI[ID]
School of Electronics Engineering, Vellore Institute of Technology (VIT University), Vellore 632014, India

Corresponding author: S. Kalaivani (kalaivani.s@vit.ac.in)

ABSTRACT Spectral unmixing in hyperspectral images involves determining endmembers and their associated abundance maps. The endmember estimate is extremely important in the processing of high resolution hyperspectral data. This study provides a unique automatic method for extracting endmembers by integrating fuzzy clustering and a spectral-matching approach. The number of endmembers in an image is estimated in the first stage using the Hysime algorithm. Data are subsequently classified using a fuzzy c-means algorithm, which determines the grade of membership values for each data point. A threshold operation on membership values is used to select a collection of pixels as target pixels. Spectral matching aids in the selection of target pixels and searches for a specific endmember within a cluster. Endmember bundles are extracted from target pixels and compared with ground truth data using a spectral angle mapper. The performance of the proposed technique was evaluated in two ways: directly on full hyperspectral data and on dimension-reduced data by employing one simulated and two real datasets. The mean spectral angle and root mean square error were used as performance indicators. Furthermore, the accuracy of extracted endmembers was validated by creating abundance maps using a fully constrained least square technique, and the results were analyzed.

INDEX TERMS Hyperspectral image, spectral unmixing, endmember estimation, fuzzy clustering, spectral matching, abundance maps.

I. INTRODUCTION
Imaging spectrometers, particularly those on the ground or in the air, offer scene data in the form of a band of planes known as a hyperspectral cube or hyperspectral images. There are four forms of hyperspectral image data extraction: categorization, endmember extraction, and spectral unmixing, target detection, and change detection [1]. An image includes the radiance value collected in one plane for all pixels in a scene at a single wavelength [2]. Almost all fields, agriculture [3], mining and geology [4], environmental monitoring [5], chemical detection [6], and astronomy, employ hyperspectral image analysis [7]. In hyperspectral photographs, the concept of unmixing is introduced by low spatial and high spectral resolution. Estimating the number of endmembers in a hyperspectral image is a crucial first step in any unmixing chain. Numerous existing algorithms underes-

timate this number due to the significant linkages observed in spectroscopic data sets. Many popular endmember estimate algorithms use connections to determine the dimension of the linear subspace containing the data [8], [9]. One of the most popular approaches [10] is the minimum error identification of hyperspectral signals (HySime). The goal of unmixing is to separate the endmembers (materials in a picture) from their associated fractional abundances (area coverage) [11]. The ratio of reflectance to emittance as a function of wavelength is known as an endmember or spectral signature. There is no such thing as an ideal spectral signature plot, and variations occur due to atmospheric adjustments, sensor noise, location, and material composition, among other reasons [12]. Mixed pixels are created when the pixel size is sufficiently large to cover more than one type of endmember. In spectral unmixing, the mixing and light interaction characteristics lead to two mathematical models, the linear mixing model (LMM) and nonlinear mixing model (NLMM). The two models are distinguished by the presence of pure pixels in an area and the

effects of multiple scattering [13]. A majority of nonlinear unmixing models are macroscopic, with the exception of radiative transfer models (e.g., the Hapke Model). Components are expected to be pure and distributed uniformly across the field of vision in LMM. In NLMM, the components are substantially intermingled [14]. Nonlinear unmixing is a difficult algorithm, as it requires thorough previous knowledge of the mixed materials and the nonlinear function of the mixed environment. Numerous strategies for linear spectral unmixing were developed due to this constraint, rather than using nonlinear spectral unmixing [15]. In the guise of a neural network, autoencoders are designed based on deep learning for blind hyperspectral unmixing [16]. The linear mixture model effectively achieves blind hyperspectral unmixing by implicitly imposing certain architectural limitations on the network. Research results proved that a more advanced encoder does not always produce superior outcomes. Regarding nonlinear hyperspectral unmixing, a unique unsupervised neural network based approach was devised by Shahid and Schizas [17]. As customary in hyperspectral unmixing, the characteristics of hyperspectral image components with increased distinction in the kernel space have been efficiently used toward estimation of endmember abundances, leading to higher precise endmember estimation.

Some approaches extract only endmembers, whereas others extract both endmembers and abundances simultaneously [18]. The suggested effort focuses entirely on endmember extraction. Various endmember algorithms include the pixel purity index (PPI) [19], vertex component analysis (VCA) [20], simplex identification via split augmented Lagrangian (SISAL) [21], successive projection algorithm [22], and simplex volume minimization (SVM) [23]. Despite the fact that PPI is the simplest algorithm among other geometrical approaches, it has one fundamental flaw: it does not use successive nulling to detect a pure pixel. VCA is based on decreasing or increasing the volume subject to find the endmember.

NFINDR is a straight forward dynamic and prominent algorithm that fails in the presence of noise [24]. When the mixing among pixels is high, statistical approaches, in particular minimum volume transform non-negative matrix factorization (MVC-NMF) [25], is the best iterative algorithm to apply for the extraction of endmembers. Geometrical approaches extract endmembers based on pure pixel assumption and choose vertices of simplex or convex regions as endmembers. In addition, there are chances of pure endmembers being present inside the region. One way to overcome this limitation is to denote simplex or convex regions as clusters [12]. Statistical approaches-based endmember extraction methods, such as independent component analysis (ICA) and dependent component analysis (DECA), are good alternatives to geometrical methods. However, their computational complexity is high, which limits their application in unmixing [12], [26]. Therefore, a clustering-based algorithm is capable of providing better results compared to conventional

methods. Due to limited spatial resolution, it is difficult to obtain pure pixels directly from hyperspectral images. Cluster analysis can be used to identify pure pixels in a mixed pixel environment [27] using fuzzy c-means (FCM) [28], KP means [29], and weighted fuzzy c-means clustering [30] approaches. These methods estimate endmembers and abundances in a parallel manner. Clustering methods differ in their initialization of parameters and minimization of the objective function to yield optimal results [31]. Subspace learning is the most important task toward the estimation of endmembers in hyperspectral images. Recently, orthogonal subspace projection combined with Gauss-Seidel alternating learning direction of multipliers [32] has been developed to find a more suitable subspace representation to extract endmembers. Another efficient method involves a non-convex framework derived from alternating direction of multipliers, designed to determine an optimal subset of spectral signatures in a spectral library to address the nonlinear unmixing problem [33]. In comparison to subspace learning methods, tensor-based methods are more appropriate to solve the unmixing problem in hyperspectral images. Tensors are highly effective in unmixing, as they represent the multi-linear interaction among materials and multiple light scattering effects in a more natural and structural manner. For example, non-negative tensor factorization based nonlinear unmixing [34] imposes a nuclear norm on abundance and nonlinear interaction maps to improve the nonlinear unmixing performance. Finally, a deep learning approach, which currently attracts more attention, employs an autoencoder in the network architecture to solve the unmixing problem in hyperspectral images. A cycle consistency algorithm designed to address the unmixing problem by learning two cascaded autoencoders in an end-to-end fashion with preservation of high-level semantic information was shown to perform better than existing approaches [35]. Multimodal unmixing proposed in [36] uses hyperspectral images and the attention map derived by LiDAR to aid the autoencoder network to differentiate endmembers with similar materials. A fully automatic network architecture [37] combines channel configuration obtained from hyperspectral images and the evolutionary algorithm with additional computational constraints into networks to achieve flexible convolution kernel search by evaluating unmixing results of different architectures in the SuperNet. Deep learning algorithms must be designed in parallel to estimate the number of endmembers, spectral signatures, and abundance maps. A more intelligent and automated approach for diverse hyperspectral remote sensing applications is required [38]. Keeping in mind the above-mentioned approaches, their various advantages, and the challenges they face, a novel method has been proposed by the authors for extracting endmembers by combining clustering and spectral-matching criteria. This approach has also been tested on a dimension-reduced dataset [39]. Because hyperspectral images are rich in spectral information, highly correlated and redundant bands must be removed to reduce

the storage needed to store and transmit data, complexity, and computation time. Dimensionality reduction, also known as band selection, is an optional step, which when employed speeds up the subsequent processing [11]. Principal component analysis (PCA) and linear discriminant analysis (LDA) techniques are applied on the higher-dimensional data to reduce its dimension.

This study proposes a novel automatic endmember extraction method combining fuzzy clustering and the spectral-matching algorithm. Fuzzy c-means clustering (FCM) is employed to identify target pixels, whereas the spectral-matching algorithm is employed to extract pure endmembers. This algorithm is applied on both the full hyperspectral data and the dimensionality-reduced data. The performances of both scenarios are assessed.

II. PROBLEM STATEMENT

Most existing endmember extraction algorithms were devised based on pure pixel assumption in remote sensing images. This is not true for many datasets, as pixels in the hyperspectral image are highly mixed in general. An alternative approach is to estimate the set of purified pixels from mixed pixels in the hyperspectral image. Statistical approaches are not based on pure pixel assumption, but the need of detailed prior knowledge and the high computational cost limits the usage of these approaches for large datasets. Few of the algorithms in the literature assume that an endmember lies on the vertices of simplex or convex regions. However, it is important to consider that an endmember can also be present inside the region. Classical methods extract endmembers from single standard spectrum assigned to a particular pixel. Consequently, these methods ignore the severe effects of intra- and inter-class variability occurring due to variations in the illumination, environment, and atmospheric and temporal conditions in hyperspectral images. The resulting variation in the endmember spectral signature is not accounted for, such that unmixing can lead to poor accuracy of estimated abundance fractions [11]. Therefore, the challenges in existing algorithms include estimating the set of purified pixels from mixed pixels, representing simplex or convex regions as clusters, and extracting endmembers from endmember bundles to account for endmember variability in hyperspectral images. To overcome these challenges, a novel method is proposed combining fuzzy clustering and spectral matching. The hyperspectral data is represented as different clusters, with the assumption that each cluster denotes an endmember. The grade of membership values of fuzzy clustering is used to identify a set of pixels as target pixels, which are more likely to represent a single endmember. Endmember bundles are generated from these sets of pixels, and a single endmember is extracted with the use of spectral matching. Endmember bundles automatically accounts for the endmember variability, and precise endmember estimation leads to more accurate abundances.

In this study, we formulate a novel automatic endmember extraction method that combines fuzzy clustering and a spectral-matching algorithm. The contributions of our work are as follows.

- The proposed method automatically and efficiently extracts endmembers from endmember bundles using fuzzy clustering and spectral matching in hyperspectral images. The endmember bundles automatically take into account the spectral variability [40], resulting in more accurate abundances [11].
- It works pixel-wise and converges iteratively to an endmember with the help of the grade of membership values.
- It avoids identification of a noisy pixel as a pure pixel in two ways. (a) The grade of membership values assist in finding a homogeneous region. ''Homogeneous'' here means that there is no variance, indicating that all pixels are same, and that there are no noisy pixels present. (b) The spectral-matching parameter will be high when the noisy spectra deviate more than the real, thus avoiding making the noisy pixel an endmember [41].
- Finally, the performance of the proposed method has been further investigated by generating abundance maps from the extracted endmembers [42] and using ablation studies.

III. PROPOSED METHOD

Spectral mixing of pixels in hyperspectral images induces loss of important spectral features of the material needed for efficient discrimination. Further, it results in poor intra-class variability of different materials. This study proposes a method to identify an endmember to account for the intra-class variability and enable selection of spectrally pure pixels by combining FCM and spectral matching. The block diagram illustrating the methodology is shown in Figure 1.

Let $Y = \{Y_1, Y_2, Y_3 \ldots Y_R\}$ be the hyperspectral data with $'\mathbf{R}'$ pixel vectors and $'B'$ number of spectral bands. Then, any pixel $'y'$ in the hyperspectral image can be modeled as a pixel vector;

$$y = \sum_{i=1}^{e} A_i E_i + n \tag{1}$$

where $'\mathbf{A}'$ is the abundance vector, $'\mathbf{E}'$ is the endmember vector, $'e'$ is the number of endmembers, $'n'$ is the additive Gaussian noise.

The spectral reflectance curves are strongly correlated, resulting in a highly mixed matrix of endmembers. This strong correlation poses a challenge in the estimation of endmembers [43], [44]. As a first step prior to endmember extraction the number of endmembers are determined by the Hysime algorithm [45], [46] and used to initialize the number of clusters in FCM.

The proposed method is tested by applying it on full band, as well as dimension-reduced data. One way to reduce its dimension is by selecting more informative bands and using only those for further processing. Band selection is the process of selecting highly dissimilar bands from strongly correlated bands and representing the data in a lower
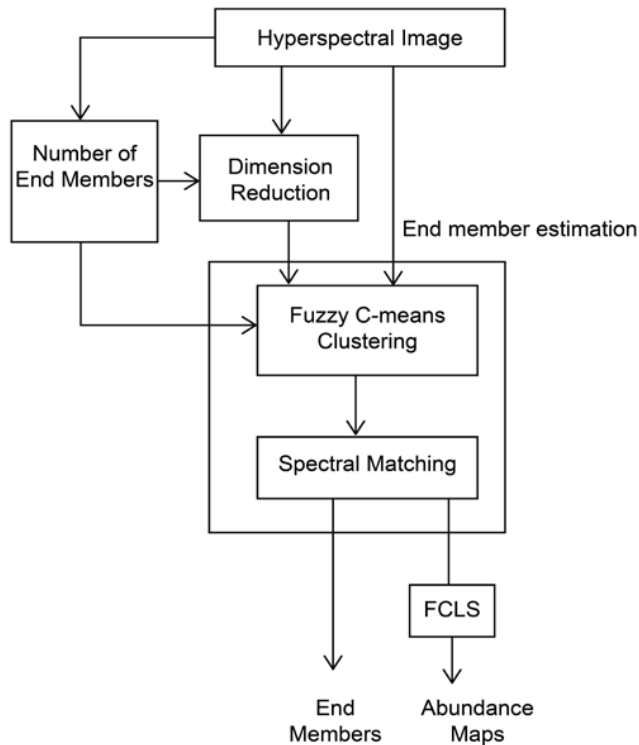
FIGURE 1. Block diagram of the proposed methodology.

FIGURE 2. Flowchart of proposed endmember estimation.

dimension [47]. Dimension-reduction methods, such as PCA [48], LDA [49], graph-based methods [50], and clustering-based methods [51] are more popular in the literature and are being used in classification tasks [52], [53], data mining [54], and unmixing applications [55]. Two well-known dimensionality reduction methods, PCA and LDA, are employed in this study. The choice of methods is done based on their performance and complexity compared to other methods. In PCA, the maximum amount of variance in high-dimensional space is preserved to the greatest possible extent, whereas LDA considerably preserves class discriminatory information in the dimension-reduction process. Moreover, LDA is an unsupervised technique that does not require any initialization [49]. Further, it is an efficient technique in that it optimizes the Fisher score to produce low-dimensional representation and shows better performance in real world remote sensing applications, mainly in terms of dimension-reduction and hyperspectral image classification [56].

After estimation of the number of endmembers, the proposed endmember extraction method classifies the data and matches the reflectance curves to extract endmembers. The flowchart of the proposed endmember estimation is depicted in Figure 2.

Existing endmember extraction methods assume that there exists at least one pure endmember in the hyperspectral data. The estimation is based on extreme pixels with a high PPI score [19], the set of pixels corresponding to larger volume NFINDR [24], convex regions covering the desired
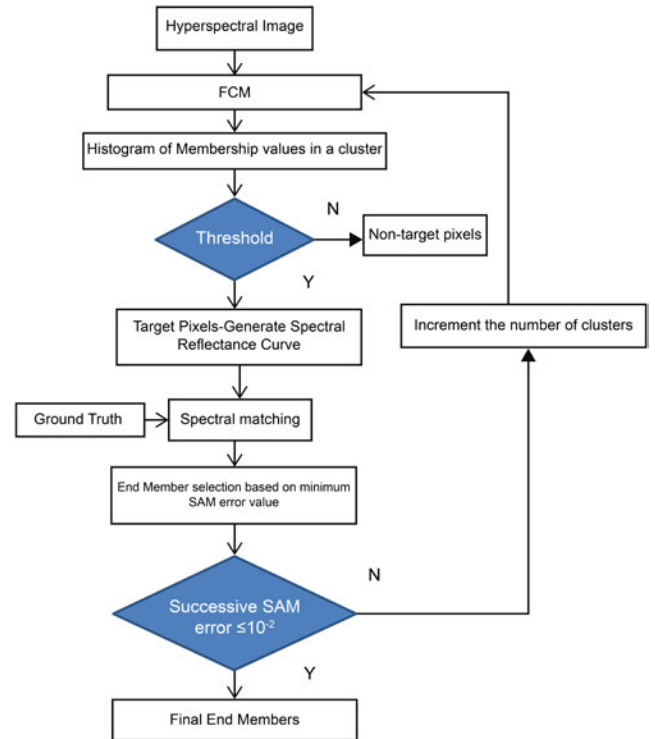
pixels SMACC [57], and minimum volume enclosing simplex MVES [23].

Most of these algorithms find the vertices as their endmembers, while failing to identify whether multiple endmembers exist in the vertex, or identify an endmember when none exists in the vertex. In the literature, the suggested approach to solve this issue is to perform piecewise operation [11] on linear models. Performing piecewise operation is similar to representing the regions as clusters instead of simplex or convex regions [27]. Clustering represents the region as different classes, while spectral-matching searches for pure pixels inside the cluster and removes the wrong identification of vertex pixels as endmembers.

Crisp classification or k-means results in a binary classification and fails to identify endmembers in a mixed pixel environment. The FCM has the advantage of providing soft class membership values with high intra- and inter-cluster similarity. FCM even works when a particular endmember does not occupy a major area in an image [58]. FCM is chosen to classify hyperspectral data, as it is more flexible in assigning the membership of each pixel to a cluster during clustering iterations compared to classical clustering methods. FCM assigns the "e" proportion of relevance to "e" classes for each pixel in the image. This feature allows reconsideration of pixel membership to image classes in further iterations of the algorithm and illustrates more appropriately the natural aspect of uncertainty existing in the data [59], [60]. This helps identify the target pixels of endmembers to be extracted.

TABLE 1. Complete algorithm.

Complete Algorithm	Proposed Method
Step 1	Input: Hyperspectral Image $Y \equiv \{y_1, y_2, ... y_R\}$
Step 2	Estimate the number of endmembers $'e'$ using Hysime algorithm
Step 3	Reduce the dimension of the original data from $'B'$ to $'e'$ using PCA and LDA.
Step 4	Perform fuzzy clustering and spectral matching on full band ($'B'bands$) and on dimension reduced data of size $'e'$ bands to extract endmembers.
Step 5	Generate abundance maps from extracted endmembers using FCLS.

TABLE 2. Real hyperspectral dataset.

Parameters	Jasper Ridge	Samson
Spatial Size	100X100	95X95
Spatial Resolution	9.46nm per pixel	9.46nm per pixel
Total bands	224	156
Wavelength Range	380nm --2500nm	401nm --889nm

FCM classifies the data cube (full hyperspectral and dimension-reduced data) into a number of clusters similar to the number of endmembers $'e'$ with random initializations. The fuzzy clustering allows pixels to have membership values denoting similarity with cluster centroids [61].

Mathematically, the LMM in Equation (1) is modified to identify target pixels using fuzzy clustering as:

$$F = \sum_{i=1}^{C} \left(\sum_{n=1}^{d} U_{in}^2 \| y_n - A_i E_i \|_2^2 \right) \tag{2}$$

Subject to $\sum_n U_{in} = 1$ and $U_{in} \in [0, 1], 0 \leq U_{in} \leq 1$

Where

d number of data points
c number of clusters
y_n n^{th} data point
U_{in} Membership value of nth data point in i^{th} cluster
m degree of fuzziness

Thus, a pixel may belong to more than one cluster with varying membership values [58]. The membership values or degree of similarity is used to find target pixels that have a higher probability to be of a single material or an end member in hyperspectral images. To identify the homogeneous region (assumed to be the noise-free region) and to group more similar pixels, a simple thresholding operation is performed on the histogram of GOM values.

The histogram of GOM values is plotted for a cluster.

$$H_i = hist \left(U_{ij} \right)_{C_n} \tag{3}$$

Then, the threshold value is obtained from H_i using the expression

$$T_{mf} = \frac{H_{i_{min}} + H_{i_{max}}}{2} \tag{4}$$

The T_{mf} metric is used to sort pixels with in a cluster C_n into target and non-target pixels. The reflectance curve is obtained from the spatial location of all target pixels.

TABLE 3. Performance measure.

Parameter	Mathematical Formulae	Definition
Root Mean Square Error(S-RMSE)	$S - RMSE$ $= \sum_{i=1}^{p} \sqrt{(1/N(\|s_g - s_i\|)^2)}$	Measure of pixel-wise error vales between GT and extracted spectral signatures.
Mean Spectral Angle Distance (M-SAD)	$M - SAD$ $= \frac{1}{N} \cos^{-1} \frac{(s_g, s_i^t)}{(\|s_g\|. \|s_i^t\|)}$	Measure the mean of SAD of all the endmembers. SAD gives the distance between extracted spectral signature and GT spectral signature as an angle.
Root Mean Square Error(A-RMSE)	$A - RMSE$ $= \sum_{i=1}^{p} \sqrt{(1/N(\|a_g - a_i\|)^2)}$	Measure of pixel-wise error values between GT and extracted abundance maps.
Mean Abundance Angle Distance (M-AAD)	$M - AAD$ $= \frac{1}{N} \cos^{-1} \frac{(a_g, a_i^t)}{(\|a_g\|. \|a_i^t\|)}$	Same as M-SAD but calculated for abundance maps,

The extracted endmembers are automatically matched with library reflectance curves with the help of spectral-matching algorithms [41].

Spectral-matching methods are the simplest and most efficient for identifying a pure pixel in a mixed pixel environment compared to conventional methods [41]. Spectral-matching measures aid in the selection of target pixels and searches for a specific endmember within a cluster. A deterministic spectral-matching parameter spectral angle mapper (SAM) is used to identify the target endmember. SAM treats the unknown spectra and ground truth spectra as pixel vectors and measures angle between them. If the angle is small, the two spectra are more similar. The spectrum of a material, characterized by the presence of absorption features, is used for accurate matching. SAM averages out the absorption features for efficient discrimination. The SAM parameter is chosen owing to its invariance to scale and illumination, computational simplicity, speed, and availability in image processing packages [62]. In this study, the SAM defined in Equation (5) is utilized as spectral-matching parameter to measure the similarity between target spectra and ground truth (GT) spectra.

The SAM between target spectra S_t and GT spectra S_g is expressed as

$$SAM = acos \frac{\sum S_t S_g}{\sqrt{S_t^2} \sqrt{S_g^2}} \tag{5}$$

A small SAM value indicates that the particular target vector is closer to the GT vector or library vector. Initially, with $'e'$ number of clusters, the endmembers are identified based on the SAM error value. Then, by increasing the number of clusters, an endmember in a particular category from multiple target pixels is decided as the final one if the
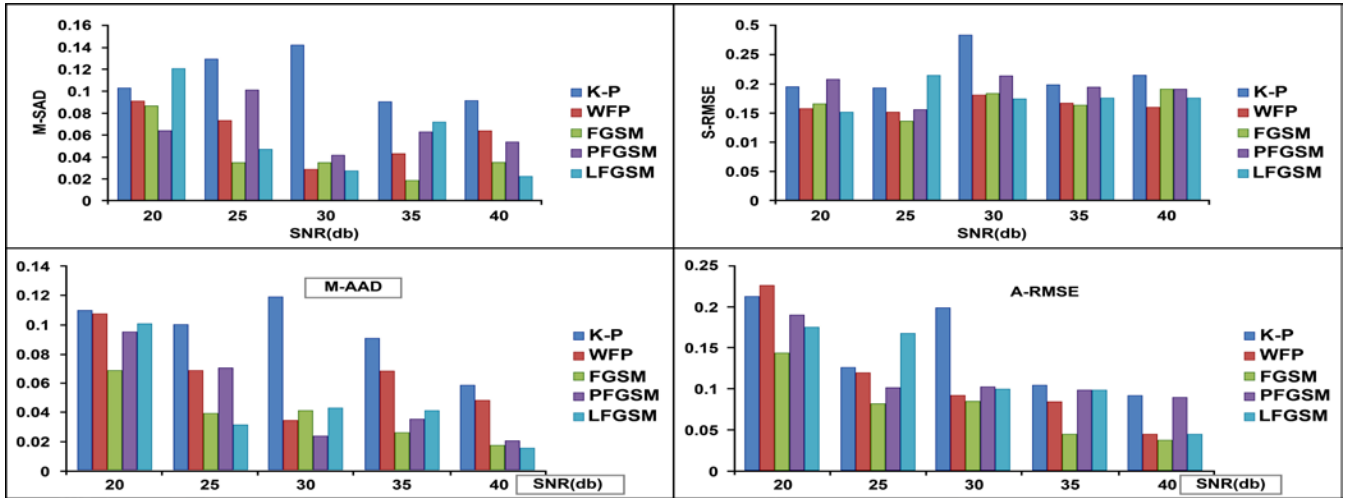
FIGURE 3. Performance measure comparison results for clustering-based methods. M-SAD, S-RMSE metrics for endmembers and M-AAD, A-RMSE metrics for abundances. The proposed methods' metric values are lower than those of WFP, K-P methods. FGSM produced minimum SAD and AAD error values in overall.
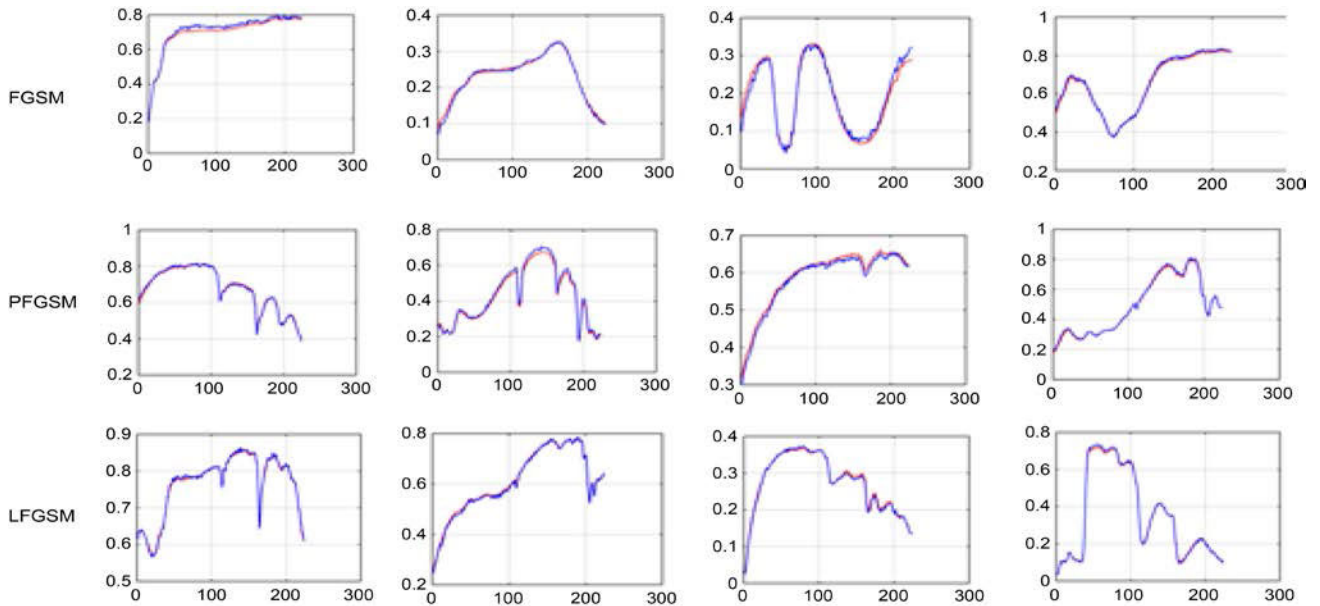

FIGURE 4. Experimental results of proposed methods for random inputs-FGSM, PFGSM, LFGSM (simulated data, SNR = 30 dB). Red indicates library spectra, and blue indicates extracted endmember. Proposed methods FGSM, PFGSM, LFGSM endmembers are more similar to library spectra. (X-axis-Wavelength, Y axis-Reflectance).

successive SAM error value is 10^{-2}. This method aims at estimating only endmembers, as good endmember estimation helps obtain accurate abundances [11]. Abundance maps can be generated with help of the fully constrained least square (FCLS) algorithm [42].

A. ABUNDANCE MAP GENERATION

Clustering-based algorithms simultaneously compute endmembers and their corresponding fractional abundances. These values may be negative and may lie on the boundary of the region leading to inaccurate results. The direct estimation of endmember and abundance from averaging of mixed

pixels leads to a biased estimation. Thus, both endmember estimation and abundance map generation are interrelated to produce finer results. Therefore, the proposed method aims to extract only endmembers from the endmember bundles obtained by increasing the number of clusters. Abundance maps are generated by applying the more popular algorithm FCLS using the estimated endmembers.

The unconstrained solution to generate fractional abundance can be expressed as,

$$A \approx \left(E^T E \right)^{-1} E^T Y \qquad (6)$$

TABLE 4. Performance measures SAD, S-RMSE-Jasper Ridge Image − SNR = 30.37 dB.

Methods	SAD				S-RMSE			
	Tree	Water	Dirt	Road	Tree	Water	Dirt	Road
VCA	0.1845	0.3187	0.1798	0.1628	0.2548	0.2748	0.2265	0.2857
NFINDR	0.1676	0.2514	0.2523	0.1022	0.2896	0.417	0.2138	0.2832
NMF	0.2596	0.3395	0.1606	0.1945	0.2155	0.3257	0.2068	0.2917
MDA	0.1601	0.2129	0.1941	0.1268	0.2027	0.3343	0.2447	0.3307
KP	0.1102	0.1568	0.1304	0.1121	0.2664	0.2147	0.2787	0.2964
WFP	0.0952	0.1865	0.1124	0.0802	0.2512	0.3124	0.2112	0.1987
FGSM	0.0403	**0.0693**	0.1112	**0.0503**	0.1765	0.2245	0.1965	0.1587
PFGSM	**0.0324**	0.1022	0.1499	0.0928	**0.0989**	**0.1968**	0.1002	0.1121
LFGSM	0.0556	0.2542	**0.0912**	0.1224	0.1224	0.2254	**0.0965**	**0.1024**
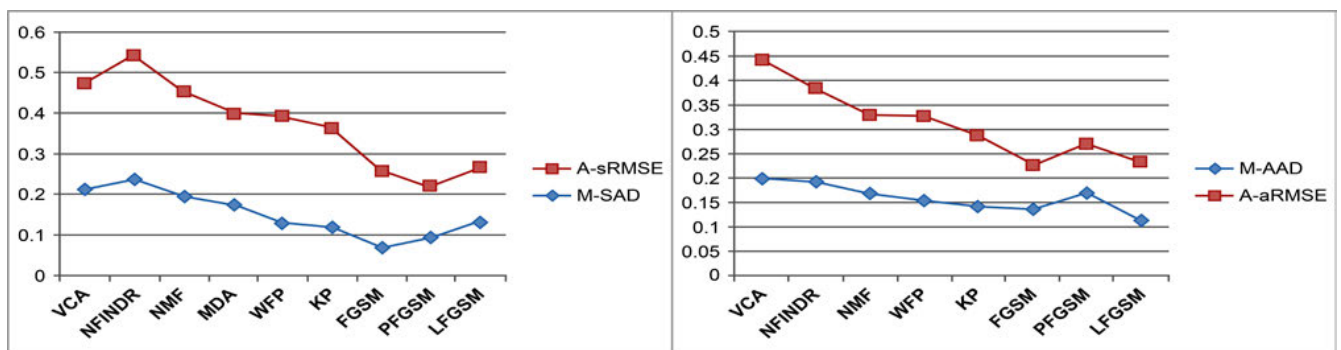
FIGURE 5. Performance measures (M-SAD, M-AAD, A-sRMSE, and A-aRMSE). Smaller value indicates better performance for all the parameters. Clustering methods results are with minimum SAD and AAD error values compared to non-clustering methods. Proposed Methods FGSM, PFGSM, LFGSM achieved minimum errors in overall.

where E is the estimated endmember, and Y is the original hyperspectral data under two constraints.

Summing to one

$$\sum_{i=1}^{e} A_i = 1, \left\{ (Y - AE)^T \ (Y - AE) \right\}$$

$$\text{Positivity} \ \sum_{i=1}^{p} A_i > 0, \left\{ (Y - AE)^T \ (Y - AE) \right\} \quad (7)$$

The complete workflow of the framework is explained through its algorithm presented in Table 1.

IV. RESULTS AND DISCUSSION

The proposed method has been implemented in MATLAB R2020a S/W and experimented on simulated data and two real hyperspectral datasets (refer Table 2).

To evaluate and estimate the performance of the proposed method, it is compared with four non-clustering-based

approaches VCA [20], NMF [25], NFINDR [24], maximum distance analysis (MDA) [9] and two clustering-based approaches WFP [30], KP means [29]. Three variant models are developed, and their results are compared with the above-mentioned methods. The methods are FGSM on full hyperspectral data, PFGSM on PCA based dimension-reduced data and LFGSM on LDA-based dimension-reduced data.

The quality metrics used to illustrate performance evaluation are listed in Table 3. Smaller values indicate better performance for all performance measures.

A. EXPERIMENT 1. TEST ON SIMULATED DATA

The first experiment was conducted on simulated data of 100×100 size with 224 bands generated by randomly selecting four endmembers from the USGS spectral library and highly mixed by applying mean filter. Then, the zero mean
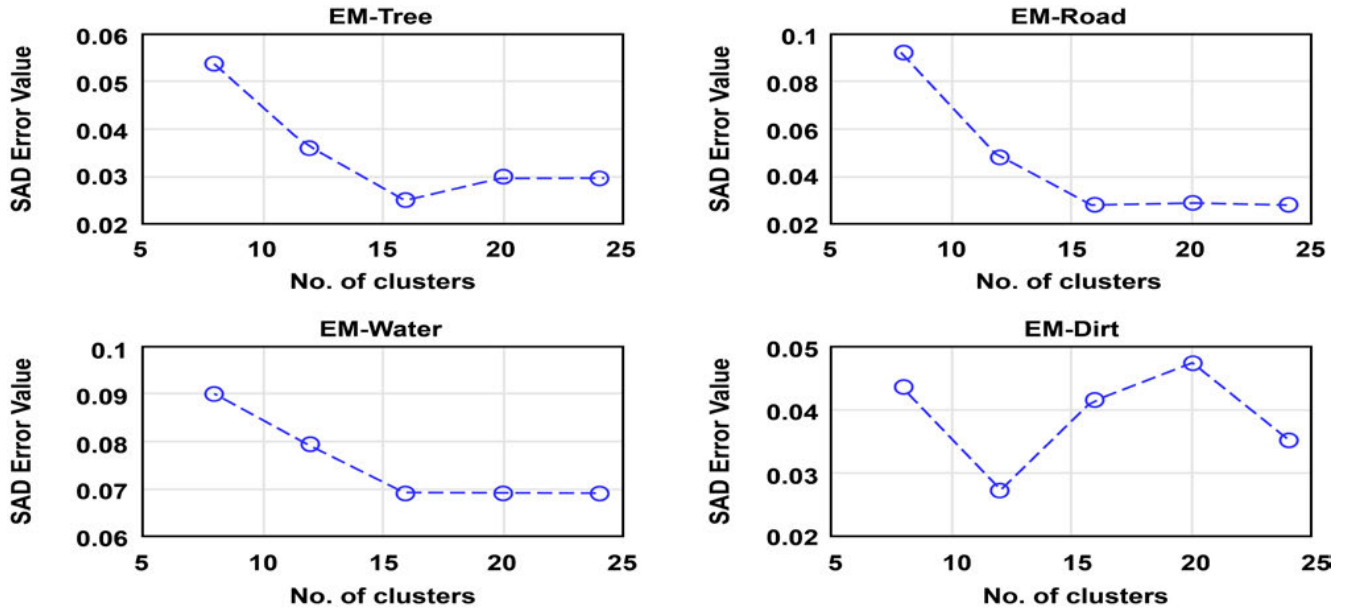
FIGURE 6. Spectral angle mapper error values of endmembers for various values of clusters.
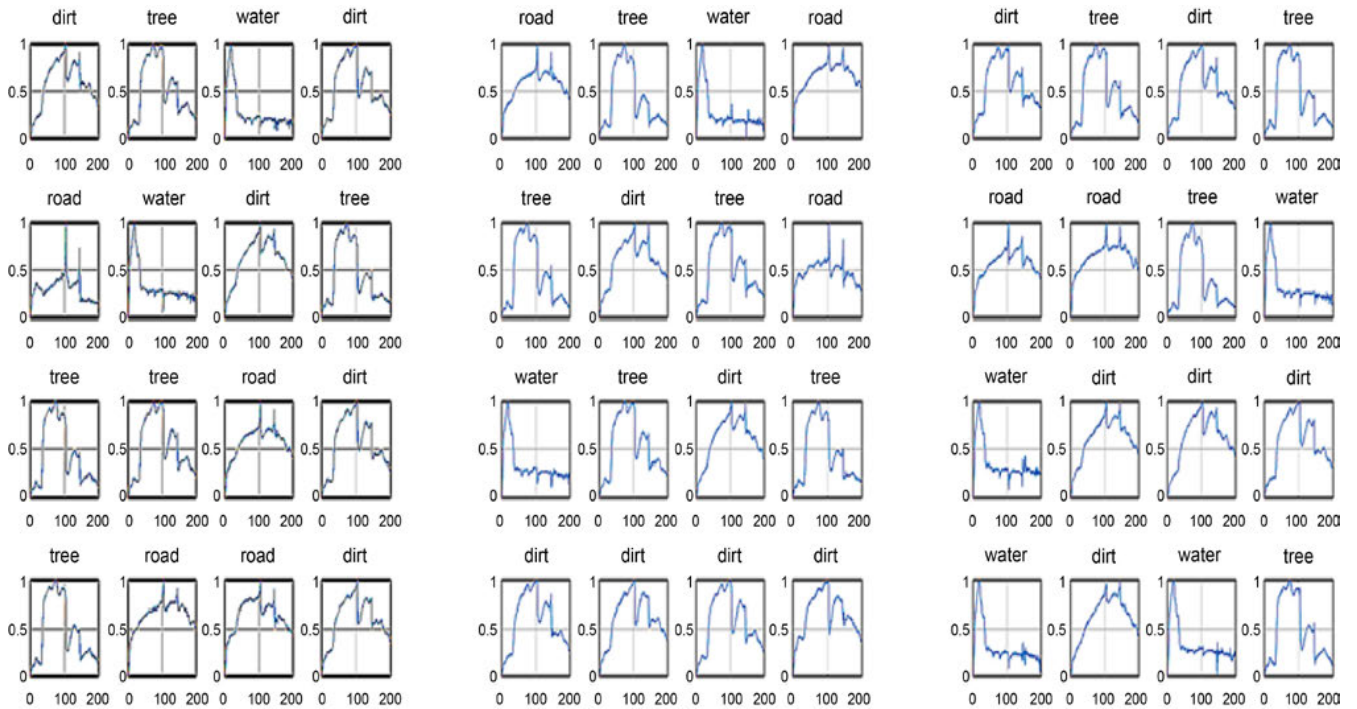

FIGURE 7. Spectral signatures obtained from target pixels in a cluster-Jasper Ridge image.

Gaussian noise with the same variance is added to all bands to further degrade the data. The various SNR values chosen to analyse the performance of the methods are 20, 25, 30, 35, and 40 dB. Most methods, especially all non-clustering methods, perform well when the noise variance is low i.e., at SNR = 35 or 40 dB.

The performance of different methods at various SNR values is displayed in Figure 3. Performance metrics indicate that in general, clustering-based methods are producing lower error results than non-clustering-based methods. Among non-clustering-based methods, MDA seems to perform better when compared to its counterparts. FGSM is capable of
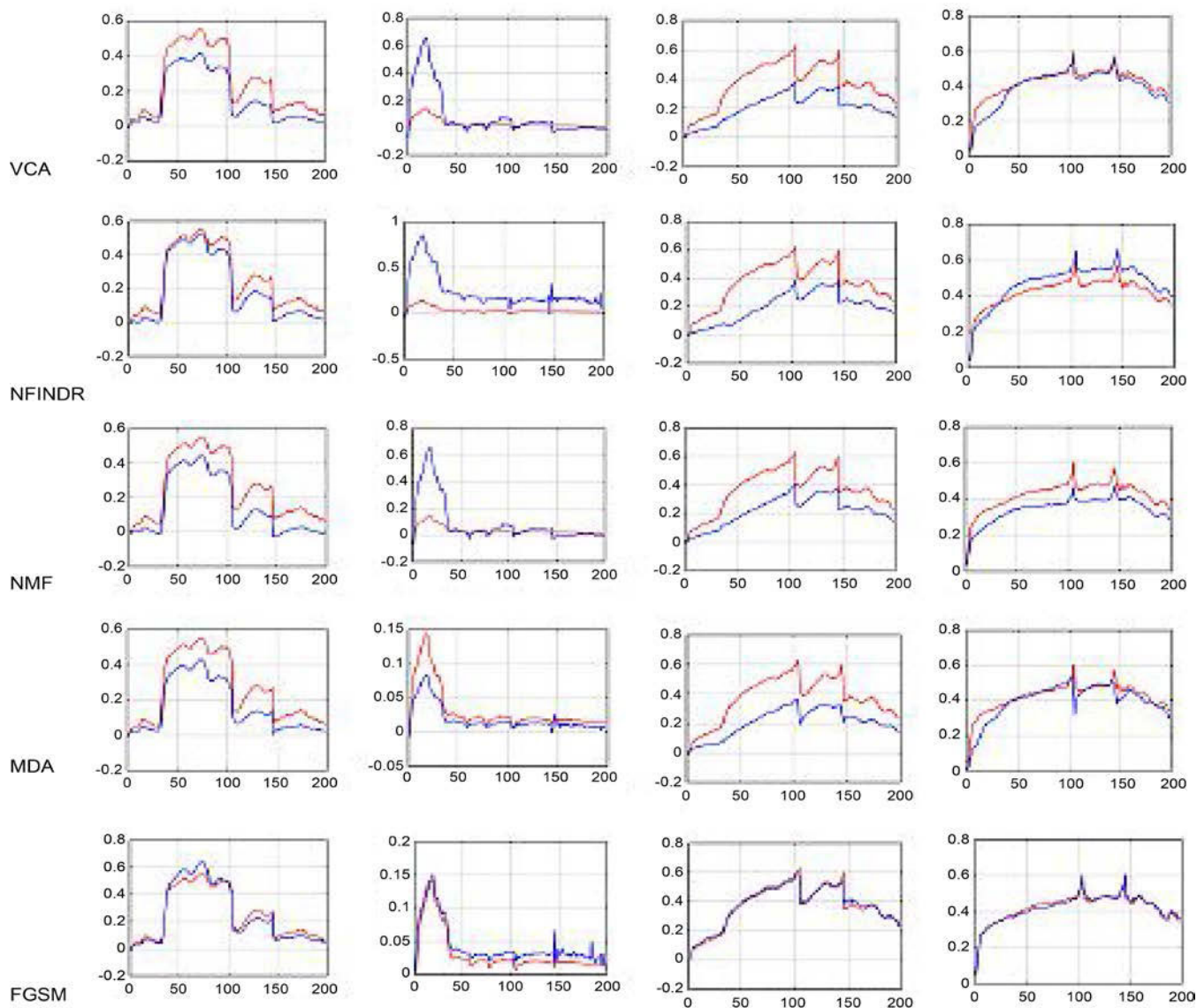
FIGURE 8. Experimental results of non-clustering methods and proposed FGSM method (Jasper Ridge Image). Red indicates ground truth, while blue depicts the extracted endmember. FGSM endmembers are more similar to GT endmembers. Particularly, the "water" endmember extracted in FGSM compared well to other methods. The remaining three extracted endmembers are similar to the GT. (X axis-Wavelength, Y axis-Reflectance).

producing comparable results with clustering-based approaches WFP and K-P means.

In the case of SNR = 20 dB, FGSM and PFGSM produced minimum error values in comparison to other methods. The next smallest values were produced by WFP, K-P, MDA, and LFGSM respectively.

In the case of SNR = 25 dB, VCA, NFINDR sometimes identify all endmembers or may miss one endmember, and similar results were obtained with SNR = 20 dB. In summary, FGSM achieved minimum error values and the next minimum error value obtained for the proposed variant model LFGSM followed by WFP, PFGSM, K-P, and MDA consecutively. In Experiment 1, the degradation of images due to varied amounts of noise is taken into account. The algorithm has

been tested on simulated data with varying levels of noise, and the results are promising, as mentioned in the Results and Discussion sections.

In summary, both for endmember estimation and abundance map generation, the proposed method is capable of producing minimum error values or comparable results to the WFP method among clustering-based approaches and to the MDA among non-clustering-based methods. The extracted endmembers exhibit spikes in the case of SNR=20 dB for non-clustering-based methods VCA, NFINDR, indicating that they fail to extract endmembers; whereas FGSM and its proposed variant methods are capable to extract smooth endmembers and are shown in Figure 4.
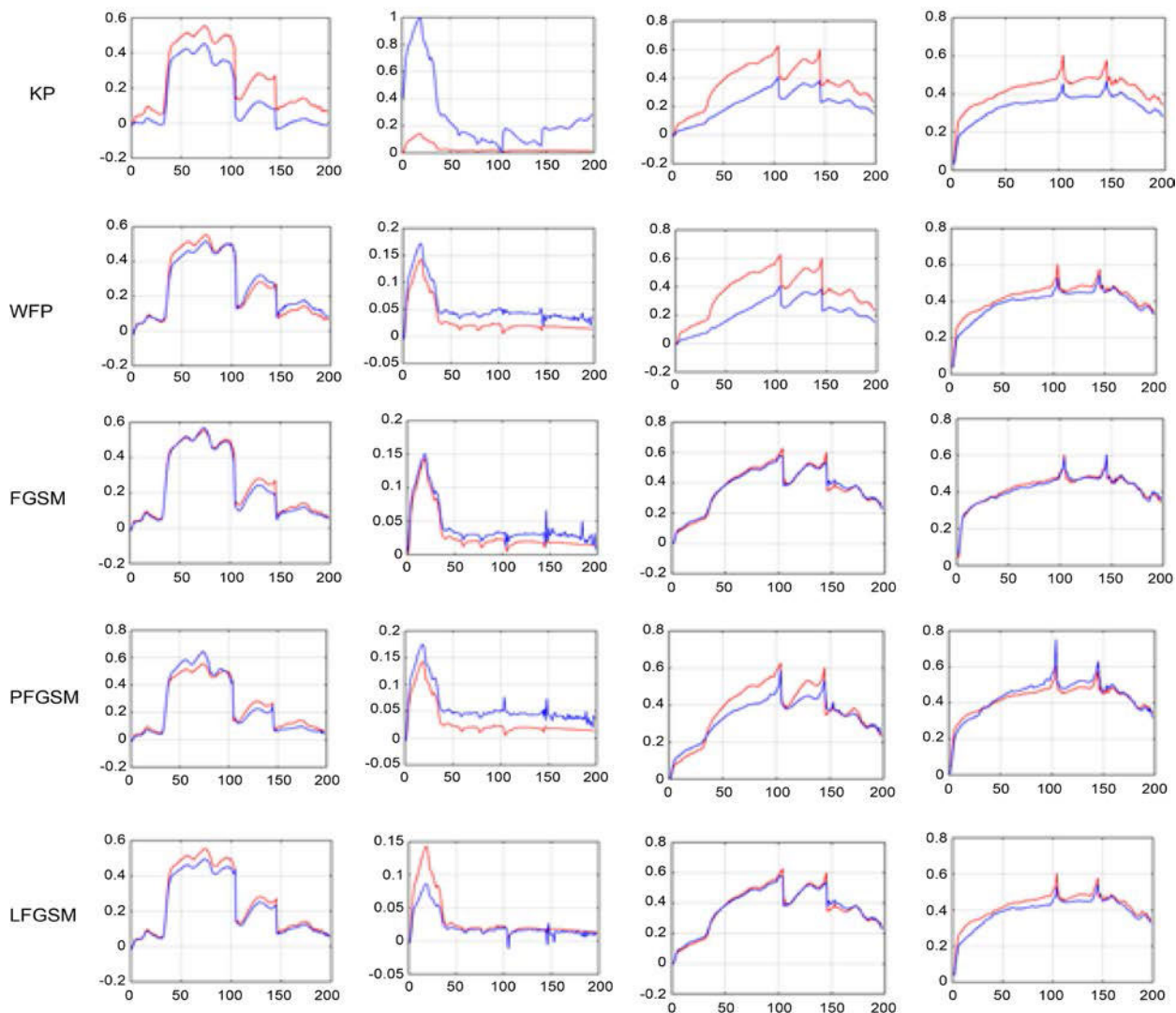
FIGURE 9. Experimental results of clustering methods and proposed methods (Jasper Ridge Image). Red indicates ground truth, while blue depicts the extracted endmember. The proposed methods FGSM, PFGSM, LFGSM extracted endmembers are more similar to the GT compared to other methods. (X axis-Wavelength, Y axis-Reflectance).

When SNR exceeds 30 dB, most methods perform satisfactorily. Nevertheless, in this case, the proposed method achieves the minimum error compared to other methods, as displayed in Figure 3.

B. EXPERIMENT 2: TEST ON REAL DATA 1

A Jasper Ridge image was adopted as real data 1, whose specifications are listed in Table 2. The number of endmembers and noise of an image are estimated using the Hysime algorithm. Then, the performances of the proposed methods are evaluated with the use of GT information available.

The four endmembers ′e′ are Tree, Water, Dirt and Road. All the four endmembers are extracted with minimum error by the proposed FGSM, PFGSM, and LFGSM methods (Table 4). Sometimes, VCA and NFINDR fail to extract one endmember and the results were shown here when all the endmembers are extracted. VCA, NFINDR, and NMF

methods extracted three endmembers with minimum error, but with a larger deviation with respect to the GT data for water endmembers. The reflectance of the water is high for VCA and NFINDR methods due to the twofold wrong identification of an endmember and due to random initialization [24]. FGSM and MDA results are more comparable among non-clustering-based methods. Existing clustering-based methods such as WFP and K-P perform better than non-clustering methods. The FGSM method on full hyperspectral data achieved superior results to other methods. The minimum error values (M-SAD, S-RMSE) yielded by this method are plotted in comparison with WFP, K-P means and PFGSM, LFGSM methods in Figure 5. Evidently, with ′e′ number of bands, PFGSM and LFGSM methods produced comparable results to FGSM, WFP, K-P means clustering methods. FGSM is easy to implement and less expensive when compared to WFP, K-P means.
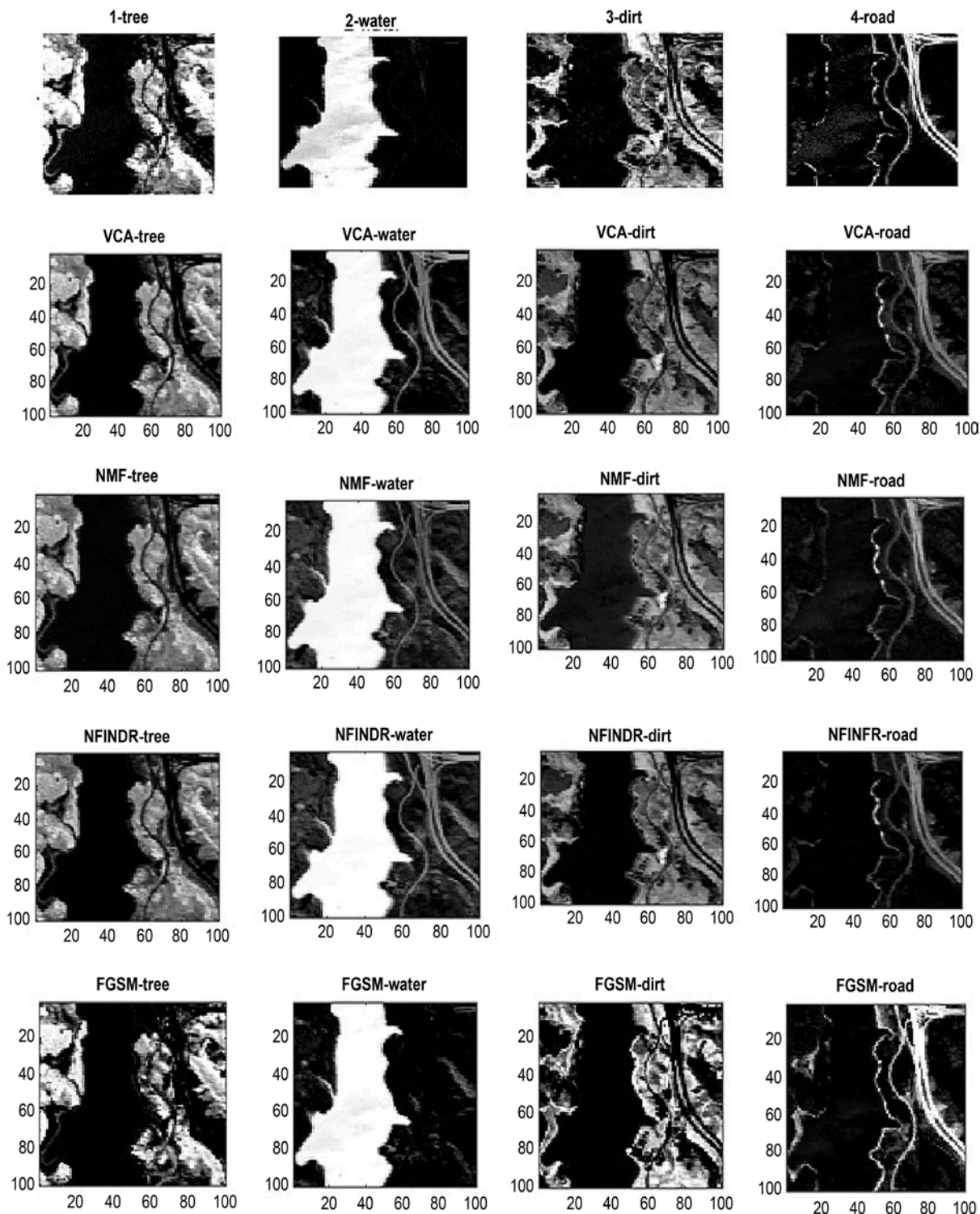
FIGURE 10. Abundance maps obtained for non-clustering methods and proposed FGSM method. FGSM maps are more similar to the ground truth map (particularly the background area of the water map).

C. SAM ERROR VALUES FOR VARYING CLUSTER SIZE

In the FGSM process, initially clustering is performed directly on original data, and $'e'$ numbers of clusters are obtained. In each cluster, target pixels are identified based on threshold membership values. For various values of $'e'$ starting from $'2e'$ to $'5e'$, the corresponding minimum SAM error values are determined. The plot results in Figure 6 show that the error decreases until 4e clusters and becomes more or

TABLE 5. Performance measures AAD, A-RMSE-Jasper Ridge Image – SNR = 30.37 dB.

Methods	AAD				A-RMSE			
	Tree	Water	Dirt	Road	Tree	Water	Dirt	Road
VCA	0.1973	0.2285	0.1254	0.1698	0.3451	0.375	0.3551	0.4556
NFINDR	0.2057	0.2419	0.1957	0.1254	0.2752	0.4297	0.5347	0.5289
NMF	0.1947	0.1688	0.1735	0.1365	0.2002	0.321	0.3441	0.4505
KP	0.1395	0.1965	0.1325	0.1498	0.3102	0.3587	0.2987	0.3356
WFP	0.1125	0.1687	0.1198	0.1654	0.2534	0.2963	0.2814	0.2987
FGSM	**0.0856**	**0.0759**	0.1866	0.1924	**0.1455**	**0.1223**	0.2514	0.3841
PFGSM	0.183	0.0964	0.2133	0.1843	0.3101	0.1521	0.3214	0.2965
LFGSM	0.1112	0.1384	**0.1108**	**0.094**	0.1956	0.2241	**0.2877**	**0.2254**

TABLE 6. Performance measures SAD, S-RMSE-Samson Image – SNR = 32.68 dB.

Methods	SAD			S-RMSE		
	Rock	Tree	Water	Rock	Tree	Water
VCA	0.0445	0.1698	0.2165	0.1533	0.0965	0.5089
NFINDR	0.0433	0.1545	0.8254	0.1313	0.1654	0.5784
NMF	0.0655	0.1204	0.338	0.0872	0.0621	0.4867
MDA	0.0503	0.1128	0.1361	0.1622	0.0658	0.5238
KP	0.0901	0.1428	0.2563	0.1264	0.0825	0.3965
WFP	0.0721	0.1104	0.1968	0.0541	0.1098	0.4696
FGSM	0.0335	0.1231	**0.0335**	**0.0765**	**0.0548**	**0.0539**
PFGSM	**0.0173**	0.1728	0.1528	**0.0686**	0.0758	**0.067**
LFGSM	0.1448	**0.1009**	**0.0813**	0.1339	**0.0514**	**0.0398**

less stable. Therefore, the stopping criterion is fixed based on successive SAM error values for a particular endmember. Spectral signatures obtained from a few target pixels are shown in Figure 7. The GT and extracted endmembers using the proposed method are plotted in Figures 8 and 9, respectively.

In terms of the abundances displayed in Figures 10 and 11, the same inferences are achieved with the help of parameters AAD, M-AAD and A-RMSE. As the number of extracted endmembers becomes more exact, so do the abundances [11]. The FGSM method generates multiple signatures for a single endmember and extracts the final signature from the

endmember bundles. It may provide more accurate endmember estimates and thereby yield abundances highly similar to GT [63]. The abundance maps error values are displayed in Table 5. Smaller AAD values are obtained for the proposed methods compared to others, indicating that the proposed endmember extraction method is good at generating more accurate smooth fractional abundances.

D. EXPERIMENT 3: TEST ON REALDATA2
Real dataset 2 is a Samson image with only three endmembers, namely rock, tree, and water. A procedure similar to the one above-mentioned one is applied to the datasets
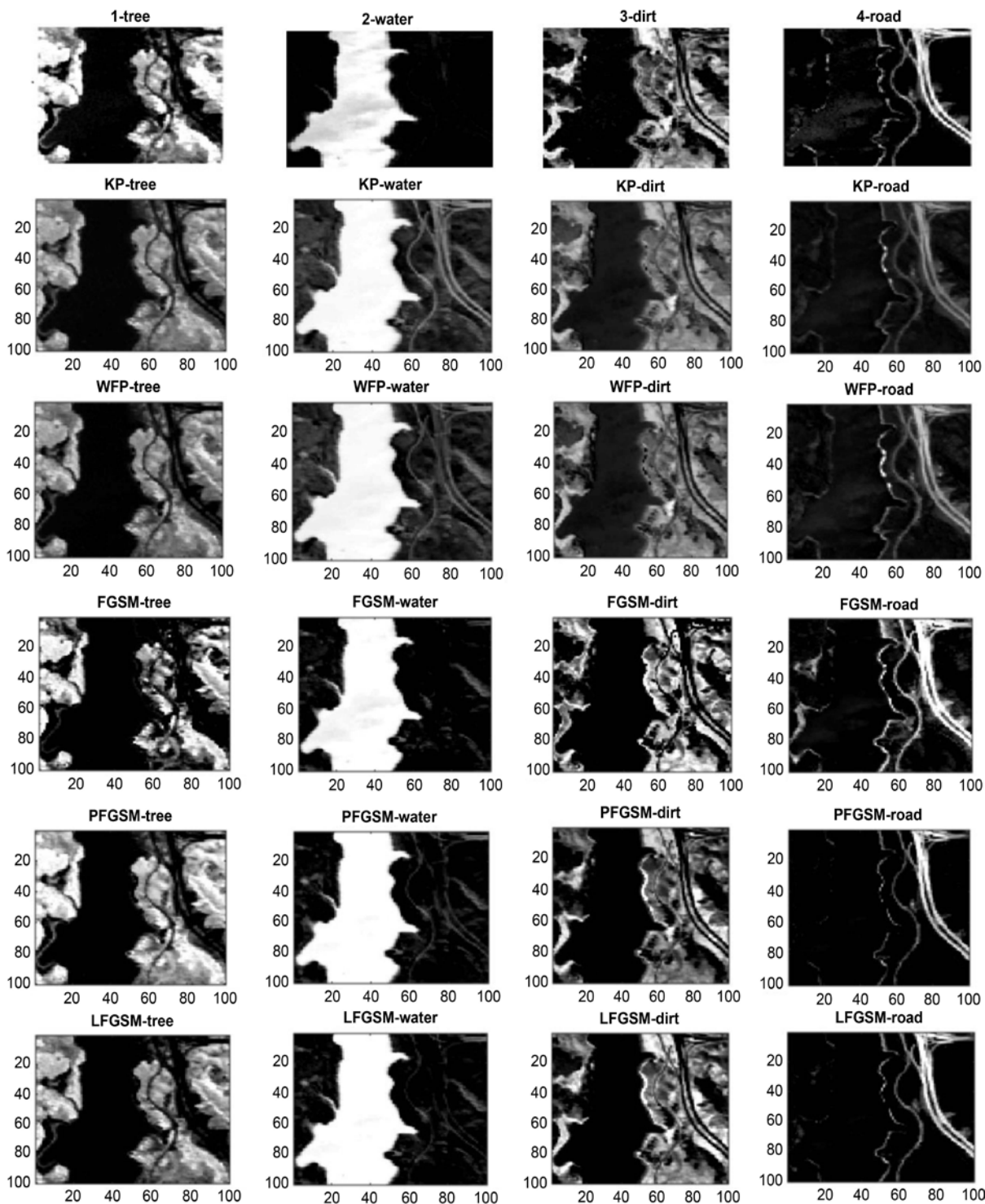
FIGURE 11. Experimental results of abundance maps obtained for clustering methods. Water and road abundance maps are similar to the ground truth for proposed methods (FGSM, PFGSM, and LFGSM).

to obtain M-SAD and S-RMSE for endmembers (refer to Table 6) and M-AAD, A-RMSE for abundance maps. All three endmembers are extracted with minimum M-SAD and S-RMSE values for FGSM, PFGSM, and LFGSM methods. The water endmember fails to be extracted accurately in all

methods except the proposed methods and MDA is shown in Figures 12 and 13. The results are shown for the case of all the three-endmember extraction for VCA and NFINDR methods. M-SAD and S-RMSE error values are lower for FGSM, and comparably better results were achieved with the minimum
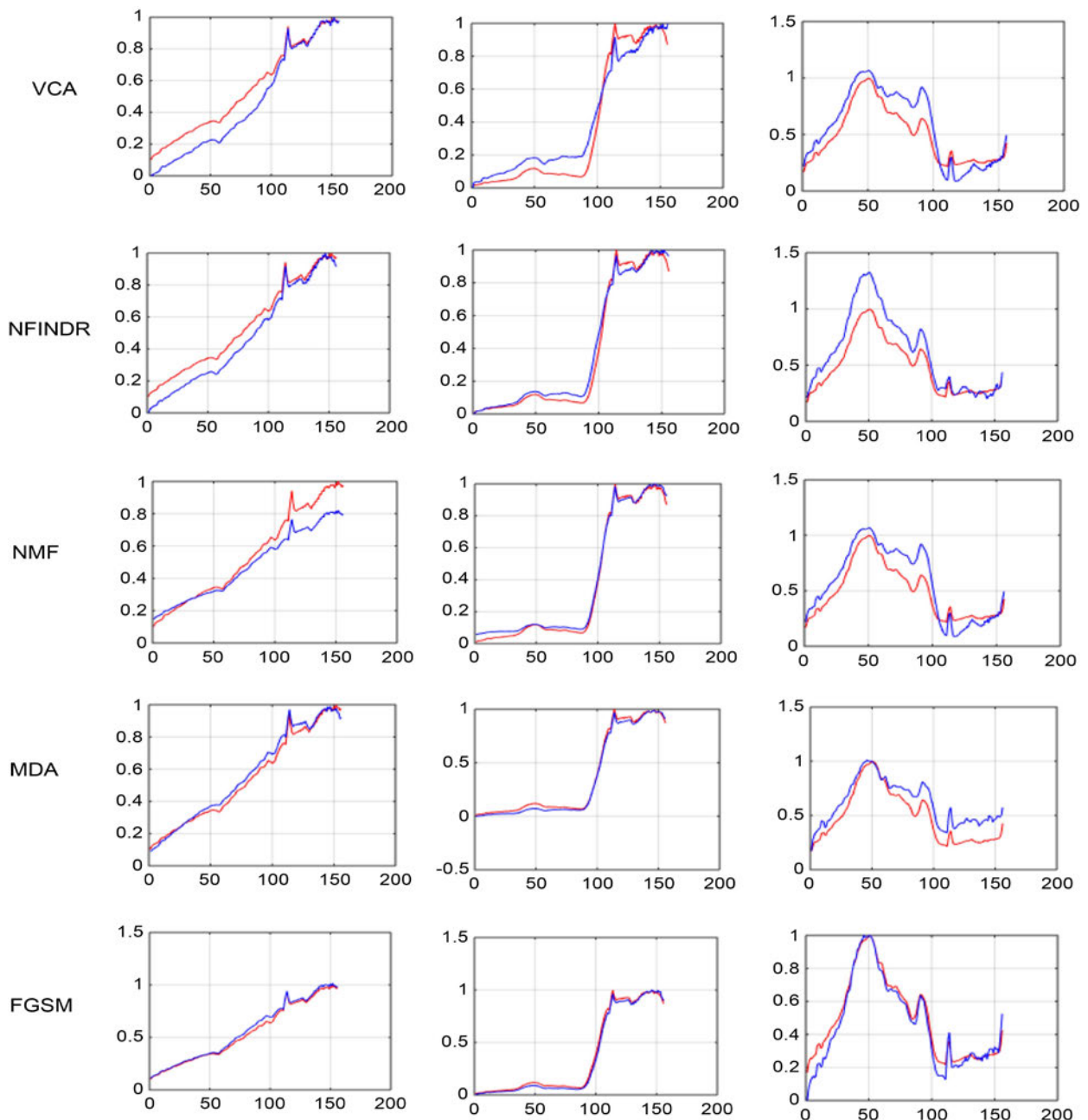
FIGURE 12. Spectral signature results of non-clustering and FGSM methods. The red line denotes the ground truth, and blue line denotes the extracted endmember. All three extracted endmembers are similar to the GT in the FGSM method. (X axis-Wavelength, Y axis-Reflectance).

number of bands in PFGSM and LFGSM, as depicted in Figure 14.

The main precise estimation of endmembers leads to more accurate abundance maps, as indicated by the M-AAD values listed in Table 7. The proposed FGSM yields results comparable to other clustering methods, such as WFP and K-P means. M-AAD and A-RMSE values also indicate consistent solutions obtained between estimated and GT information. The average values of the performance metrics are displayed in Figure 14, where clustering-based methods achieved minimum error values when compared to non-clustering-based

methods. In a nutshell, FGSM and its variant methods achieved minimum error values in the estimation of endmembers and abundance map generation.

E. COMPUTATION TIME
The proposed method does not involve complex calculation, as it only combines two algorithms of fuzzy clustering and spectral matching. As a result, the computational complexity is solely determined by FCM complexity $O(ndc^2i)$ (n-number of data points, d-dimension of the data, c-number of clusters, i-number of iterations). The performance of the
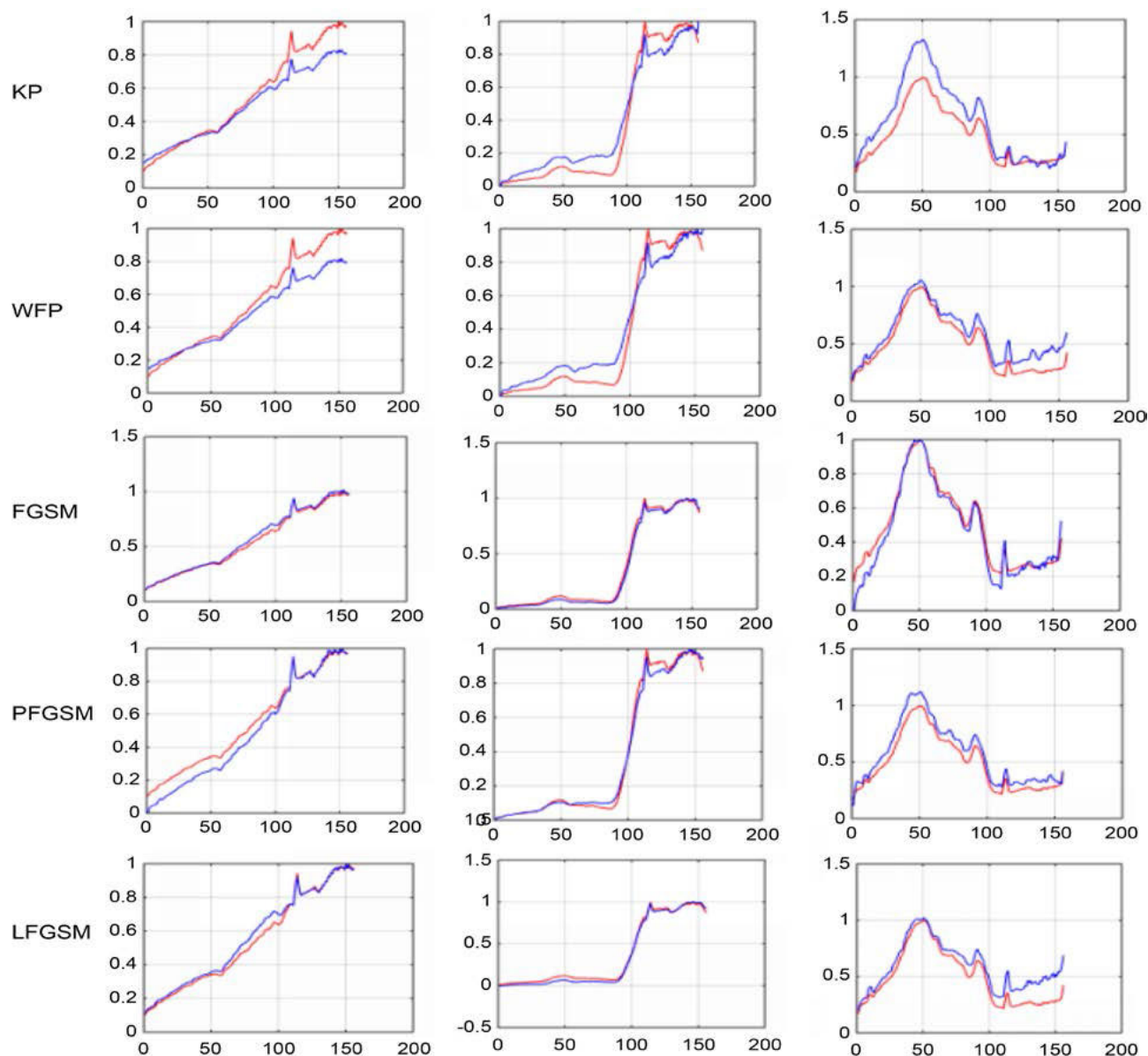
FIGURE 13. Spectral signature results of clustering methods. Red line denotes ground truth, while blue line depicts the extracted endmember. Overall, FGSM performs superior extraction, followed by WFP, PFGSM, LFGSM, and K-P, consecutively (X axis-Wavelength, Y axis-Reflectance).

proposed method is found to be good for both the original and dimension-reduced data. Therefore, for the dimension-reduced data, the complexity will be comparatively lower.

The running time of the experiments is evaluated on a computer with intel i5-6200, X64 based processor, 2.4 GHz CPU and 8 GB random access memory. Figure 15 presents the average computing time of the Jasper Ridge and Samson datasets. Because FGSM is implemented with full bands, its computation time is higher than with other methods. The computation time of the proposed methods PFGSM and LFGSM with dimension-reduced bands are acceptable compared to other methods. Further, the proposed methods extract endmembers from endmember bundles, such that the time

requirement is lower compared to other clustering and non-clustering-based methods.

F. ABLATION ANALYSIS

Increasing the number of clusters and checking for the successive SAM error improves the performance of the proposed method. This can be analyzed with the help of performance measures M-SAD and average A-sRMSE. Table 8 shows the analysis of the algorithm with fixed and varying number of clusters with successive error for the two real datasets used in the Results and Discussion section.

FGSM with a fixed number of clusters produces larger errors compared to the proposed methods that increase the

TABLE 7. Performance measures AAD, A-RMSE-Samson Image − SNR = 32.68 dB.

Methods	AAD			A-RMSE		
	Rock	**Tree**	**Water**	**Rock**	**Tree**	**Water**
VCA	0.265	0.2511	0.4235	0.3711	0.3029	0.6792
NFINDR	0.2454	0.2491	0.3554	0.3784	0.3021	0.6831
NMF	0.2393	0.2487	0.3818	0.2903	0.2879	0.6836
KP	0.2365	0.1665	0.3981	0.2998	0.2864	0.6015
WFP	0.2309	0.2397	0.3718	**0.2895**	**0.2711**	0.6799
FGSM	0.2259	**0.1531**	0.2409	0.4511	0.2904	0.4191
PFGSM	0.2329	0.1675	**0.2164**	0.4575	0.3081	**0.3783**
LFGSM	**0.1985**	0.1595	0.2239	0.3788	0.2999	0.3942
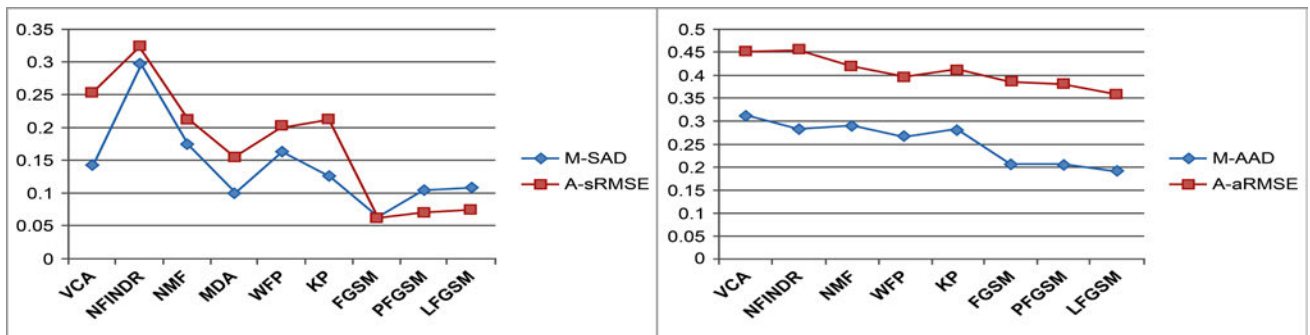
FIGURE 14. Performance measures (M-SAD, M-AAD, A-sRMSE, and A-aRMSE)-Samson Image. Clustering methods results are minimum compared to non-clustering methods in terms of both SAD and AAD. Proposed methods FGSM, PFGSM, LFGSM achieved minimum error values in overall.

TABLE 8. Ablation analysis-real datasets.

Methods	Jasper Ridge		Samson	
	M-SAD	A-sRMSE	M-SAD	A-sRMSE
FGSM-with fixed number of clusters	0.2214	0.2578	0.1935	0.2014
FGSM-incrementing the number clusters and successive SAM error	0.0677	0.1866	0.0633	0.0617
PFGSM- incrementing the number clusters and successive SAM error	0.0943	0.1263	0.1143	0.0704
LFGSM- incrementing the number clusters and successive SAM error	0.1322	0.1314	0.1090	0.0750

number of clusters and search for successive minimum SAM error.

G. DISCUSSIONS

The proposed methods employ a simple approach to extract endmembers by combining fuzzy clustering and spectral-matching algorithms. The methodology increases the number of clusters and searches for an endmember using spectral mapping to achieve better results. This causes the longer computation time of FGSM. Spectral mapping parameters, such as the SAM, spectral information divergence, and combined spectral similarity value, are used to match the extracted spectra with the GT. Each of these parameters has their own advantages and disadvantages. Few of the parameters take into account spatial characteristics only, and a few consider spectral characteristics, while they fail to consider the effects due to atmospheric and illumination conditions. Therefore, this search can be replaced by any unsupervised learning or
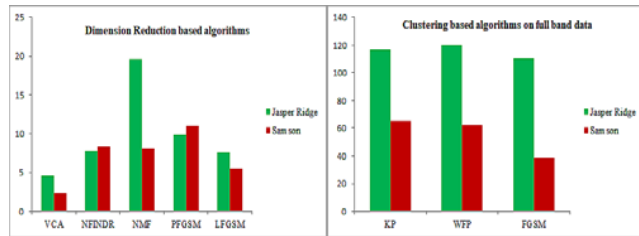
FIGURE 15. Comparison of computation time (in seconds)-real datasets.

deep learning techniques. Deep learning algorithms, such as the convolutional neural network, radial basis function, and auto encoders are used in dimension reduction and classification of hyperspectral images [64]. The same can be applied to search for an endmember in the fuzzy classified data of the proposed methods. The estimation of endmembers is a critical step in spectral unmixing, and in the classification of the hyperspectral image. Deep learning algorithms can be used to estimate the number of endmembers, spectral signatures, and abundance maps in parallel [65]. The performance of the deep learning algorithm relies on the large training samples used to train the network. In hyperspectral images, a large number of training samples must be created with the available GT spectral signatures and abundance maps. Then, a suitable convolutional neural network can be designed to estimate the number of endmembers and extract them in parallel. Future work would involve replacing spectral matching with the unsupervised learning algorithm to search for an endmember among a set of target pixels obtained through fuzzy clustering.

V. CONCLUSION

A novel automatic endmember extraction method is proposed by combining fuzzy clustering and the spectral-matching algorithm. Fuzzy clustering helps identify target pixels, followed by the extraction of pure endmembers using the spectral-matching algorithm. Fuzzy clustering assigns soft class membership values to each pixel, which helps identify it as target pixel. The spectral-matching algorithm using SAM aims to select endmembers from the target pixels. The proposed method can be implemented on full hyperspectral data, as well as on dimensionality-reduced data. The performance regarding computation time on dimensionality-reduced data is good compared to existing methods. The proposed method was tested on both simulated and real datasets. Performance metrics show that proposed methods produce superior results when compared to existing clustering and non-clustering-based methods in the presence of noise. Performance analyses on the generation of abundance maps from extracted endmembers likewise yielded efficient results in comparison with the existing state-of-the-art methods. In the future, the use of proposed endmember estimation in change detection applications can be employed to detect and analyse changes in the mangrove forest caused by natural and anthropogenic disturbances.

REFERENCES

[1] L. Zhang and B. Du, "Recent advances in hyperspectral image processing," *Geo-Spatial Inf. Sci.*, vol. 15, no. 3, pp. 143–156, Sep. 2012, doi: 10.1080/10095020.2012.719684.

[2] W.-K. Ma, J. M. Bioucas-Dias, T.-H. Chan, N. Gillis, P. Gader, A. J. Plaza, A. Ambikapathi, and C.-Y. Chi, "A signal processing perspective on hyperspectral unmixing: Insights from remote sensing," *IEEE Signal Process. Mag.*, vol. 31, no. 1, pp. 67–81, Jan. 2014, doi: 10.1109/MSP.2013.2279731.

[3] L. M. Dale, A. Thewis, C. Boudry, I. Rotar, P. Dardenne, V. Baeten, and J. A. F. Pierna, "Hyperspectral imaging applications in agriculture and agro-food product quality and safety control: A review," *Appl. Spectrosc. Rev.*, vol. 48, no. 2, pp. 142–159, Mar. 2013, doi: 10.1080/05704928.2012.705800.

[4] X. Jia, B.-C. Kuo, and M. M. Crawford, "Feature mining for hyperspectral image classification," *Proc. IEEE*, vol. 101, no. 3, pp. 676–697, Mar. 2013, doi: 10.1109/JPROC.2012.2229082.

[5] M. Moroni, E. Lupo, E. Marra, and A. Cenedese, "Hyperspectral image analysis in environmental monitoring: Setup of a new tunable filter platform," *Proc. Environ. Sci.*, vol. 19, pp. 885–894, Jan. 2013, doi: 10.1016/j.proenv.2013.06.098.

[6] R. E. Warren and D. B. Cohn, "Chemical detection on surfaces by hyperspectral imaging," *J. Appl. Remote Sens.*, vol. 11, no. 1, Feb. 2017, Art. no. 015013, doi: 10.1117/1.JRS.11.015013.

[7] E. K. Hege, D. O'Connell, W. Johnson, S. Basty, and E. L. Dereniak, "Hyperspectral imaging for astronomy and space surveillance," *Proc. SPIE*, vol. 5159, pp. 380–391, Jan. 2004, doi: 10.1117/12.506426.

[8] J. M. Bioucas-Dias and J. M. P. Nascimento, "Hyperspectral subspace identification," *IEEE Trans. Geosci. Remote Sens.*, vol. 46, no. 8, pp. 2435–2445, Aug. 2008, doi: 10.1109/TGRS.2008.918089.

[9] X. Tao, M. E. Paoletti, J. M. Haut, P. Ren, J. Plaza, and A. Plaza, "Endmember estimation with maximum distance analysis," *Remote Sens.*, vol. 13, no. 4, p. 713, Feb. 2021, doi: 10.3390/rs13040713.

[10] R. Heylen, M. Parente, and P. Scheunders, "Estimation of the number of endmembers via the hubness phenomenon," in *Proc. 8th Workshop Hyperspectral Image Signal Process., Evol. Remote Sens. (WHISPERS)*, Aug. 2016, pp. 1–4, doi: 10.1109/WHISPERS.2016.8071749.

[11] N. Keshava and J. F. Mustard, "Spectral unmixing," *IEEE Signal Process. Mag.*, vol. 19, no. 1, pp. 44–57, Jan. 2002, doi: 10.1109/79.974727.

[12] J. M. Bioucas-Dias, A. Plaza, N. Dobigeon, M. Parente, Q. Du, P. Gader, and J. Chanussot, "Hyperspectral unmixing overview: Geometrical, statistical, and sparse regression-based approaches," *IEEE J. Sel. Topics Appl. Earth Observ. Remote Sens.*, vol. 5, no. 2, pp. 354–379, Apr. 2012, doi: 10.1109/JSTARS.2012.2194696.

[13] B. Hapke, "Bidirectional reflectance spectroscopy: 1. Theory," *J. Geophys. Res., Solid Earth*, vol. 86, no. B4, pp. 3039–3054, Apr. 1981, doi: 10.1029/JB086iB04p03039.

[14] N. Dobigeon, J.-Y. Tourneret, C. Richard, J. C. M. Bermudez, S. McLaughlin, and A. O. Hero, "Nonlinear unmixing of hyperspectral images: Models and algorithms," *IEEE Signal Process. Mag.*, vol. 31, no. 1, pp. 82–94, Jan. 2014, doi: 10.1109/MSP.2013.2279274.

[15] J. Wei and X. Wang, "An overview on linear unmixing of hyperspectral data," *Math. Problems Eng.*, vol. 2020, Aug. 2020, Art. no. 3735403, doi: 10.1155/2020/3735403.

[16] B. Palsson, J. Sigurdsson, J. R. Sveinsson, and M. O. Ulfarsson, "Hyperspectral unmixing using a neural network autoencoder," *IEEE Access*, vol. 6, pp. 25646–25656, 2018, doi: 10.1109/ACCESS.2018.2818280.

[17] K. T. Shahid and I. D. Schizas, "Unsupervised hyperspectral unmixing via nonlinear autoencoders," *IEEE Trans. Geosci. Remote Sens.*, vol. 60, 2022, Art. no. 5506513, doi: 10.1109/TGRS.2021.3077833.

[18] M. R. V. Devi and S. Kalaivani, "A view on spectral unmixing in hyperspectral images," *Far East J. Electron. Commun.*, vol. 16, pp. 23–32, Apr. 2016, doi: 10.17654/EC03010023.

[19] X. Wu, B. Huang, A. Plaza, Y. Li, and C. Wu, "Real-time implementation of the pixel purity index algorithm for endmember identification on GPUs," *IEEE Geosci. Remote Sens. Lett.*, vol. 11, no. 5, pp. 955–959, May 2014, doi: 10.1109/LGRS.2013.2283214.

[20] J. M. P. Nascimento and J. M. B. Dias, "Vertex component analysis: A fast algorithm to unmix hyperspectral data," *IEEE Trans. Geosci. Remote Sens.*, vol. 43, no. 4, pp. 898–910, Apr. 2005.

[21] J. M. Bioucas-Dias, "A variable splitting augmented Lagrangian approach to linear spectral unmixing," in *Proc. 1st Workshop Hyperspectral Image Signal Process., Evol. Remote Sens.*, Aug. 2009, pp. 1–4, doi: 10.1109/WHISPERS.2009.5289072.

[22] J. Zhang, B. Rivard, and D. Rogge, "The successive projection algorithm (SPA), an algorithm with a spatial constraint for the automatic search of endmembers in hyperspectral data," *Sensors*, vol. 8, no. 2, pp. 1321–1342, Feb. 2008, doi: 10.3390/s8021321.

[23] J. Li and J. M. Bioucas-Dias, "Minimum volume simplex analysis: A fast algorithm to unmix hyperspectral data," in *Proc. IEEE Int. Geosci. Remote Sens. Symp. (IGARSS)*, Jul. 2008, p. 250, doi: 10.1109/IGARSS.2008.4779330.

[24] M. E. Winter, "N-FINDR: An algorithm for fast autonomous spectral end-member determination in hyperspectral data," *Proc. SPIE*, vol. 3753, pp. 266–275, Oct. 1999, doi: 10.1117/12.366289.

[25] X.-R. Geng, L.-Y. Ji, and K. Sun, "Non-negative matrix factorization based unmixing for principal component transformed hyperspectral data," *Frontiers Inf. Technol. Electron. Eng.*, vol. 17, no. 5, pp. 403–412, May 2016, doi: 10.1631/FITEE.1600028.

[26] M. Lv, X. Zhao, L. Liu, and L. Jing, "Discriminant collaborative neighborhood preserving embedding for hyperspectral imagery," *J. Appl. Remote Sens.*, vol. 11, no. 4, Oct. 2017, Art. no. 046004, doi: 10.1117/1.JRS.11.046004.

[27] E. A. Mylona, O. A. Sykioti, K. D. Koutroumbas, and A. A. Rontogiannis, "Spectral unmixing-based clustering of high-spatial resolution hyperspectral imagery," *IEEE J. Sel. Topics Appl. Earth Observ. Remote Sens.*, vol. 10, no. 8, pp. 3711–3721, Aug. 2017, doi: 10.1109/JSTARS.2017.2687703.

[28] M. Berman, H. Kiiveri, R. Lagerstrom, A. Ernst, R. Dunne, and J. F. Huntington, "ICE: A statistical approach to identifying endmembers in hyperspectral images," *IEEE Trans. Geosci. Remote Sens.*, vol. 42, no. 10, pp. 2085–2095, Oct. 2004, doi: 10.1109/TGRS.2004.835299.

[29] L. Xu, J. Li, A. Wong, and J. Peng, "K-P-means: A clustering algorithm of k 'purified' means for hyperspectral endmember estimation," *IEEE Geosci. Remote Sens. Lett.*, vol. 11, no. 10, pp. 1787–1791, Oct. 2014, doi: 10.1109/LGRS.2014.2309340.

[30] L. Xu, A. Wong, F. Li, and D. A. Clausi, "Extraction of endmembers from hyperspectral images using a weighted fuzzy purified-means clustering model," *IEEE J. Sel. Topics Appl. Earth Observ. Remote Sens.*, vol. 9, no. 2, pp. 695–707, Feb. 2016, doi: 10.1109/JSTARS.2015.2450499.

[31] N. Keshava, "A survey of spectral unmixing algorithms," *Lincoln Lab. J.*, vol. 14, no. 1, pp. 55–78, 2003.

[32] L. Ren, D. Hong, L. Gao, X. Sun, M. Huang, and J. Chanussot, "Orthogonal subspace unmixing to address spectral variability for hyperspectral image," *IEEE Trans. Geosci. Remote Sens.*, vol. 61, 2023, Art. no. 5501713, doi: 10.1109/TGRS.2023.3236471.

[33] L. Ren, Z. Ma, F. Bovolo, and L. Bruzzone, "A nonconvex framework for sparse unmixing incorporating the group structure of the spectral library," *IEEE Trans. Geosci. Remote Sens.*, vol. 60, 2022, Art. no. 5506719, doi: 10.1109/TGRS.2021.3081101.

[34] L. Gao, Z. Wang, L. Zhuang, H. Yu, B. Zhang, and J. Chanussot, "Using low-rank representation of abundance maps and nonnegative tensor factorization for hyperspectral nonlinear unmixing," *IEEE Trans. Geosci. Remote Sens.*, vol. 60, 2022, Art. no. 5504017, doi: 10.1109/TGRS.2021.3065990.

[35] L. Gao, Z. Han, D. Hong, B. Zhang, and J. Chanussot, "CyCU-Net: Cycle-consistency unmixing network by learning cascaded autoencoders," *IEEE Trans. Geosci. Remote Sens.*, vol. 60, 2022, Art. no. 5503914, doi: 10.1109/TGRS.2021.3064958.

[36] Z. Han, D. Hong, L. Gao, J. Yao, B. Zhang, and J. Chanussot, "Multimodal hyperspectral unmixing: Insights from attention networks," *IEEE Trans. Geosci. Remote Sens.*, vol. 60, 2022, Art. no. 5524913, doi: 10.1109/TGRS.2022.3155794.

[37] Z. Han, D. Hong, L. Gao, B. Zhang, M. Huang, and J. Chanussot, "AutoNAS: Automatic neural architecture search for hyperspectral unmixing," *IEEE Trans. Geosci. Remote Sens.*, vol. 60, 2022, Art. no. 5532214, doi: 10.1109/TGRS.2022.3186480.

[38] D. Hong, W. He, N. Yokoya, J. Yao, L. Gao, L. Zhang, J. Chanussot, and X. Zhu, "Interpretable hyperspectral artificial intelligence: When nonconvex modeling meets hyperspectral remote sensing," *IEEE Geosci. Remote Sens. Mag.*, vol. 9, no. 2, pp. 52–87, Jun. 2021, doi: 10.1109/MGRS.2021.3064051.

[39] D. Hong, L. Gao, J. Yao, B. Zhang, A. Plaza, and J. Chanussot, "Graph convolutional networks for hyperspectral image classification," *IEEE Trans. Geosci. Remote Sens.*, vol. 59, no. 7, pp. 5966–5978, Jul. 2021, doi: 10.1109/TGRS.2020.3015157.

[40] T. Uezato, M. Fauvel, and N. Dobigeon, "A multiple endmember mixing model to handle spectral variability in hyperspectral unmixing," in *Proc. 9th Workshop Hyperspectral Image Signal Process., Evol. Remote Sens. (WHISPERS)*, Sep. 2018, pp. 1–5, doi: 10.1109/WHISPERS.2018.8747110.

[41] S. Shanmugam and P. S. Perumal, "Spectral matching approaches in hyperspectral image processing," *Int. J. Remote Sens.*, vol. 35, no. 24, pp. 8217–8251, Dec. 2014, doi: 10.1080/01431161.2014.980922.

[42] D. C. Heinz and C.-I. Chang, "Fully constrained least squares linear spectral mixture analysis method for material quantification in hyperspectral imagery," *IEEE Trans. Geosci. Remote Sens.*, vol. 39, no. 3, pp. 529–545, Mar. 2001, doi: 10.1109/36.911111.

[43] R. Fernandez-Beltran, F. Pla, and A. Plaza, "Endmember extraction from hyperspectral imagery based on probabilistic tensor moments," *IEEE Geosci. Remote Sens. Lett.*, vol. 17, no. 12, pp. 2120–2124, Dec. 2020, doi: 10.1109/LGRS.2019.2963114.

[44] X. Tao, T. Cui, A. Plaza, and P. Ren, "Simultaneously counting and extracting endmembers in a hyperspectral image based on divergent subsets," *IEEE Trans. Geosci. Remote Sens.*, vol. 58, no. 12, pp. 8952–8966, Dec. 2020, doi: 10.1109/TGRS.2020.2992542.

[45] D. Baran and N. Apostolescu, "A virtual dimensionality method for hyperspectral imagery," *Proc. Eng.*, vol. 100, pp. 460–465, Jan. 2015, doi: 10.1016/j.proeng.2015.01.391.

[46] S. Sánchez and A. Plaza, "Fast determination of the number of endmembers for real-time hyperspectral unmixing on GPUs," *J. Real-Time Image Process.*, vol. 9, no. 3, pp. 397–405, Sep. 2014, doi: 10.1007/s11554-012-0276-3.

[47] M. Baisantry, A. K. Sao, and D. P. Shukla, "Band selection using combined divergence–correlation index and sparse loadings representation for hyperspectral image classification," *IEEE J. Sel. Topics Appl. Earth Observ. Remote Sens.*, vol. 13, pp. 5011–5026, 2020, doi: 10.1109/JSTARS.2020.3014784.

[48] K. Koonsanit, C. Jaruskulchai, and A. Eiumnoh, "Band selection for dimension reduction in hyper spectral image using integrated information gain and principal components analysis technique," *Int. J. Mach. Learn. Comput.*, vol. 2, no. 3, pp. 248–251, 2012.

[49] M. Chen, Q. Wang, and X. Li, "Discriminant analysis with graph learning for hyperspectral image classification," *Remote Sens.*, vol. 10, no. 6, p. 836, May 2018, doi: 10.3390/rs10060836.

[50] L. Zhang and F. Luo, "Review on graph learning for dimensionality reduction of hyperspectral image," *Geo-Spatial Inf. Sci.*, vol. 23, no. 1, pp. 98–106, Jan. 2020, doi: 10.1080/10095020.2020.1720529.

[51] S. I. Benabadji, M. S. Karoui, K. Djerriri, I. Boukerch, N. Farhi, and M. A. Bouhlala, "Unsupervised hyperspectral band selection by combination of unmixing and sequential clustering techniques," *Eur. J. Remote Sens.*, vol. 52, no. 1, pp. 30–39, 2019, doi: 10.1080/22797254.2018.1549511.

[52] P.-H. Hsu, Y.-H. Tseng, and P. Gong, "Dimension reduction of hyperspectral images for classification applications," *Ann. GIS*, vol. 8, no. 1, pp. 1–8, Jun. 2002, doi: 10.1080/10824000209480567.

[53] R. Reshma, V. Sowmya, and K. P. Soman, "Dimensionality reduction using band selection technique for kernel based hyperspectral image classification," *Proc. Comput. Sci.*, vol. 93, pp. 396–402, Jan. 2016, doi: 10.1016/j.procs.2016.07.226.

[54] O. Saini and S. Sharma, "A review on dimension reduction techniques in data mining," *Comput. Eng. Intell. Syst.*, vol. 9, no. 1, pp. 7–14, 2018.

[55] M. R. V. Devi and S. Kalaivani, "Feature extraction-based hyperspectral unmixing," in *Proc. ICTMI*, B. Gulyás, P. Padmanabhan, A. Fred, T. Kumar, and S. Kumar, Eds. Singapore: Springer, 2017, doi: 10.1007/978-981-13-1477-3_15.

[56] P. Ghamisi, N. Yokoya, J. Li, W. Liao, S. Liu, J. Plaza, B. Rasti, and A. Plaza, "Advances in hyperspectral image and signal processing: A comprehensive overview of the state of the art," *IEEE Geosci. Remote Sens. Mag.*, vol. 5, no. 4, pp. 37–78, Dec. 2017, doi: 10.1109/MGRS.2017.2762087.

[57] J. H. Gruninger, A. J. Ratkowski, and M. L. Hoke, "The sequential maximum angle convex cone (SMACC) endmember model," *Proc. SPIE*, vol. 5425, pp. 1–14, Aug. 2004, doi: 10.1117/12.543794.

[58] J. C. Bezdek, R. Ehrlich, and W. Full, "FCM: The fuzzy c-means clustering algorithm," *Comput. Geosci.*, vol. 10, nos. 2–3, pp. 191–203, 1984, doi: 10.1016/0098-3004(84)90020-7.

[59] M. B. Salem, K. S. Ettabaa, and M. S. Bouhlel, "Hyperspectral image feature selection for the fuzzy c-means spatial and spectral clustering," in *Proc. Int. Image Process., Appl. Syst. (IPAS)*, 2016, pp. 1–5, doi: 10.1109/IPAS.2016.7880114.

[60] T. Nouri, "Detection of potential gold mineralization areas using MF-fuzzy approach on multispectral data," *Geocarto Int.*, vol. 37, no. 17, pp. 5017–5040, Sep. 2022, doi: 10.1080/10106049.2021.1903575.

[61] A. Ghosh, N. S. Mishra, and S. Ghosh, "Fuzzy clustering algorithms for unsupervised change detection in remote sensing images," *Inf. Sci.*, vol. 181, no. 4, pp. 699–715, Feb. 2011, doi: 10.1016/j.ins.2010.10.016.

[62] F. A. Kruse, A. B. Lefkoff, J. W. Boardman, K. B. Heidebrecht, A. T. Shapiro, P. J. Barloon, and A. F. H. Goetz, "The spectral image processing system (SIPS)—Interactive visualization and analysis of imaging spectrometer data," *Remote Sens. Environ.*, vol. 44, nos. 2–3, pp. 145–163, May 1993, doi: 10.1016/0034-4257(93)90013-N.

[63] B. Somers, M. Zortea, A. Plaza, and G. P. Asner, "Automated extraction of image-based endmember bundles for improved spectral unmixing," *IEEE J. Sel. Topics Appl. Earth Observ. Remote Sens.*, vol. 5, no. 2, pp. 396–408, Apr. 2012, doi: 10.1109/JSTARS.2011.2181340.

[64] B. Palsson, J. R. Sveinsson, and M. O. Ulfarsson, "Blind hyperspectral unmixing using autoencoders: A critical comparison," *IEEE J. Sel. Topics Appl. Earth Observ. Remote Sens.*, vol. 15, pp. 1340–1372, 2022, doi: 10.1109/JSTARS.2021.3140154.

[65] X. Tao, M. E. Paoletti, L. Han, Z. Wu, P. Ren, J. Plaza, A. Plaza, and J. M. Haut, "A new deep convolutional network for effective hyperspectral unmixing," *IEEE J. Sel. Topics Appl. Earth Observ. Remote Sens.*, vol. 15, pp. 6999–7012, 2022, doi: 10.1109/JSTARS.2022.3200733.

M. R. VIMALA DEVI received the B.E. degree in electronics and communication from Madras University, Chennai, India, and the M.E. degree in communication systems from Madurai Kamaraj University, Madurai, India. She is currently pursuing the Ph.D. degree with the School of Electronics Engineering, VIT University, Vellore, India.

Her research interests include signal and image processing, hyperspectral data analysis, deep learning, and computer vision.

S. KALAIVANI received the B.E. degree in electronics and communication from the Government College of Engineering, Salem, India, and the M.E. and Ph.D. degrees from Anna University, Chennai, India.

She is currently a Professor with the School of Electronics Engineering (SENSE), VIT University, Vellore, India. Her research interests include medical image processing, SAR image processing, hyperspectral image analysis, and signal processing.

• • •